Next Materials 4 (2024) 100188

Contents lists available at ScienceDirect

Next Materials

journal homepage: www.sciencedirect.com/journal/next-materials

Research article

Optimizing lithium-silver alloy phases for enhanced energy density and electrochemical performance

Yuping Huang [a,c,1], Shiwei Chen [a,c,1], Jiqiong Liu [b], Yu Yang [a], Xinyu Yu [a,c], Xinchen Xu [b], Huirong Jing [a], Yunlong Guo [a], Shou-Hang Bo [c], Huanan Duan [b,*], Hong Zhu [a,*]

[a] University of Michigan–Shanghai Jiao Tong University Joint Institute, Shanghai Jiao Tong University, Shanghai 200240, China
[b] State Key Laboratory of Metal Matrix Composites, School of Materials Science and Engineering, Shanghai Jiao Tong University, Shanghai 200240, China
[c] Future Battery Research Center, Global Institute of Future Technology, Shanghai Jiao Tong University, Shanghai 200240, China

ARTICLE INFO

Keywords:
Alloy anode
Li-Ag alloy
High-energy-density battery

ABSTRACT

Lithium (Li) metal batteries though with high energy density are still facing issues like Li dendrite growth, dead Li formation, and thick solid electrolyte interphase (SEI) formation, hindering their long-term stability. Recently, Li-Ag alloys have been reported to potentially address these challenges possibly due to their superior conductivity, lithiophilicity, and mechanical stability. In the pursuit of high-energy-density batteries, Li-Ag alloys typically employ a high Li content phase (γ1). In this study, we applied density functional theory (DFT) calculations to compare the thermodynamic stability, Li adsorption, and Li diffusion of Ag-rich Li-Ag alloy within the γ1 phase (AR-γ1), Ag-poor Li-Ag alloy within the γ1 phase (AP-γ1), and pure Li. AR-γ1 showed better thermodynamic stability and improved Li adsorption and diffusion properties compared to AP-γ1 and pure Li. Electrochemical tests further confirmed the advantages of AR-γ1 in terms of electrode kinetics and cell stability compared to AP-γ1 and pure Li. Our study offers guidance for the selection of the most suitable Li-Ag alloys that can be utilized in high-energy-density lithium batteries.

1. Introduction

Li metal batteries are being praised as promising contenders for the next generation of energy storage systems due to the exceptionally low reduction potential (−3.04 V vs. SHE) and the remarkable theoretical specific capacity (3860 mAh g^{-1}) offered by Li metal anodes. [1–5] The growth of Li dendrite [6,7] and the presence of dead Li [8,9] contribute to the susceptibility of batteries to internal short circuits. Additionally, the electrolyte's severe decomposition can lead to the formation of a thicker solid electrolyte interphase (SEI). [10–12] These factors collectively present substantial challenges in ensuring the prolonged safe operation of Li metal batteries. Addressing these issues is crucial for establishing the long-term viability and safety of these batteries. To effectively address these issues, research focus has been directed towards Li alloy anodes, encompassing Li-Al, [13] Li-Mg, [14] Li-Sn, [15,16] and Li-Ag, [17–19] etc., driven by their superior properties like cost-effectiveness, [20] reduced chemical reactivity, [21] and Li storage capability. [22] Among these alloys, the adoption of Li-Ag alloy anodes emerges to be particularly promising, attributed to their facilitated phase transitions, [23] moderate chemical stability, remarkable affinity for Li (lithiophilicity), and outstanding mechanical stability. [24–27] The combination of these attributes positions Li-Ag alloy anodes as a strong and hopeful candidate for advanced alloy anode applications.

As commonly understood, the pursuit of high-energy-density batteries often involves the utilization of Li alloy anodes with high Li content. For instance, Kyotani et al. [28] discovered that Li-rich Li-Si alloy, with the composition of $Li_{21}Si_5$, serves as a Li-ion battery anode material with excellent cycling stability and energy density. Choi et al. [29] promoted stable whisker growth on Li metal electrodes by the incorporation of 1.5 at% magnesium into Li, successfully achieving dendrite suppression and enhanced energy density. Jin et al. [30] controlled Li deposition within metal film via reversible solid-solution phase transition ($Li_{20}Ag$), preventing dendrite formation. However, the aforementioned studies did not compare different alloy phases. Considering the allowed composition space of the solid-solution phase, such as the γ1 phase in Li-Ag alloy (Fig. 1a), the determination of the optimal Li content within

---

* Corresponding authors.
E-mail addresses: hd1@sjtu.edu.cn (H. Duan), hong.zhu@sjtu.edu.cn (H. Zhu).

[1] These authors contributed equally to this work and should be considered co-first authors.

https://doi.org/10.1016/j.nxmate.2024.100188
Received 5 January 2024; Received in revised form 16 February 2024; Accepted 27 March 2024
Available online 4 April 2024
2949-8228/© 2024 The Author(s). Published by Elsevier Ltd. This is an open access article under the CC BY-NC license (http://creativecommons.org/licenses/by-nc/4.0/).

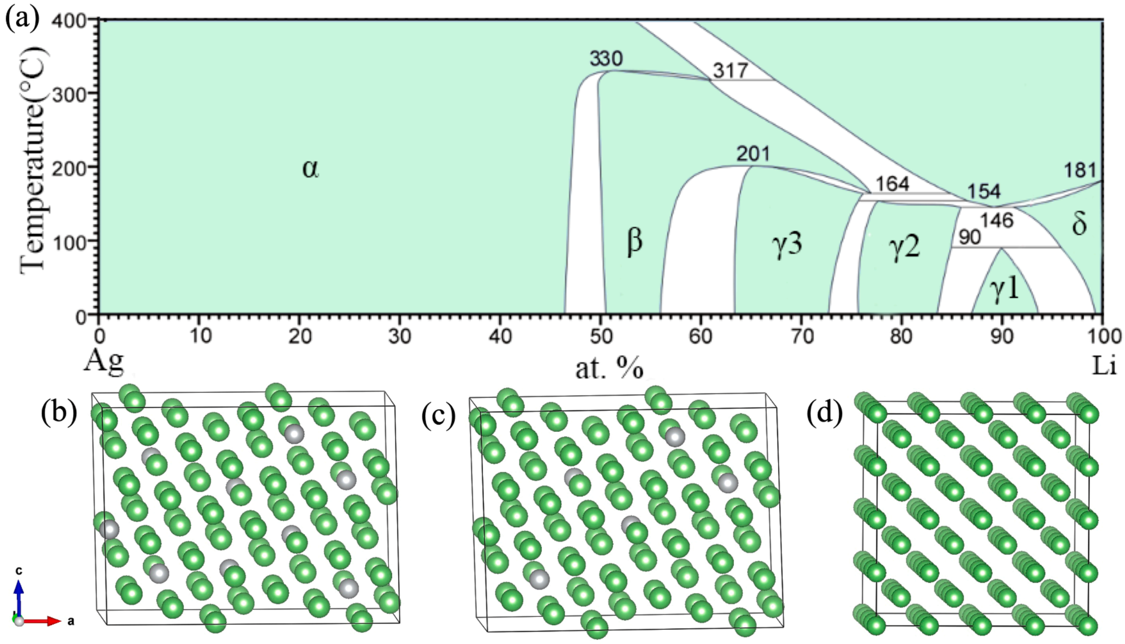

Fig. 1. The phase diagram and crystal structures of Li-Ag alloys. (a) The Li-Ag alloys phase diagram. The Li-Ag phase diagram is obtained according to the information provided in refer [49]. (b) The AR-γ1 structure. (c) The AP-γ1 structure. (d) The Li structure. The Li atoms are denoted in green and the Ag atoms in grey. The crystal structure visualizations were created using the VESTA software. [50].

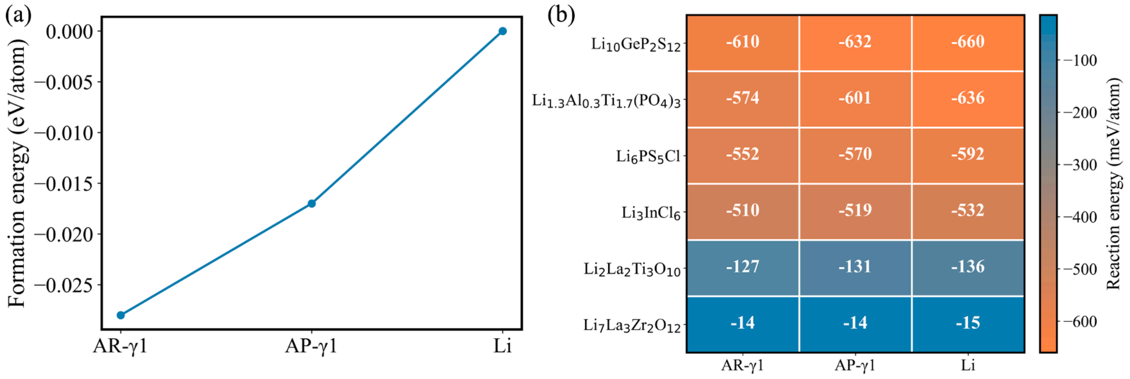

Fig. 2. The thermodynamic stability of AR-γ1, AP-γ1, and Li. (a) Formation energy and (b) Reaction energy between AR-γ1, AP-γ1, Li, and six solid-state electrolytes.

the solid-solution phase is yet to be explored. This effort aims to strike a balance between achieving high energy density and maintaining optimal electrochemical performance.

In this study, we comprehensively investigated the Ag-rich and Ag-poor γ1 solid solution phases of Li-Ag alloy anodes, namely AR-γ1 and AP-γ1, along with pure Li. Employing density functional theory (DFT) calculations, we compared the thermodynamic stability, Li adsorption energy, and Li diffusion within AR-γ1, AP-γ1, and pure Li. Subsequently, experimental validation of their electrochemical performance was conducted. Our findings demonstrate that AR-γ1 outperforms the other two phases. These findings offer valuable insights to guide the selection of Li alloy anodes with high energy density and cycling stability.

2. Computational methodology

DFT [31] calculations were executed within the Vienna Ab initio Simulation Package (VASP). [32] The interaction between ions and electrons was treated using the projector augmented-wave (PAW) method. [33,34] All calculations utilized the generalized gradient approximation Perdew–Burke–Ernzerhof (GGA-PBE) exchange and correlation functional. The wave function energy cutoff was set to 520 eV. For Brillouin zone integration, a 2 × 2 × 2 k-point mesh was utilized with the Gamma centered k-mesh. Convergence limits were set to 1×10^{-5} eV/atom for energy and 0.01 eV/Å for force calculations.

2.1. Formation energy

The thermodynamic tendency for Li to form an alloy with Ag can be evaluated using the formation energy of the Li_mAg_n alloy at 0 K, indicated as E_f as follows: [35]

$$E_f = (E(Li_mAg_n) - mE(Li) - nE(Ag)) / (m + n) \quad (1)$$

Here, $E(Li_mAg_n)$, $E(Li)$, and $E(Ag)$ are the DFT total energies of the bulk Li_mAg_n, Li, and Ag, respectively.

2.2. Vacancy formation energy

The formation energy of a Li vacancy (E^f_{vac}) [36,37] was computed based on the following equation:

$$E^f_{vac} = E_{vac} + E_{Li} - E_{bulk} \quad (2)$$

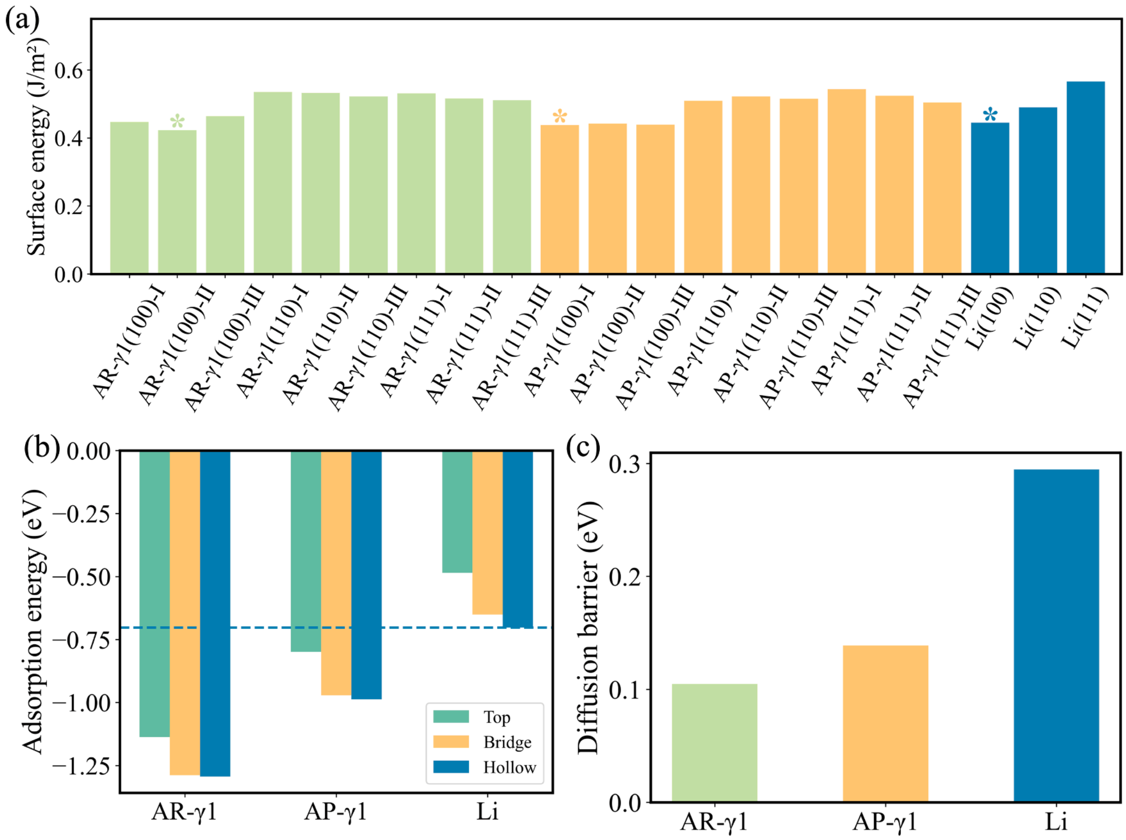

Fig. 3. A comparative analysis of AR-γ1, AP-γ1, and pure Li: (a) Surface energy, (b) Adsorption energy of Li, and (c) Li diffusion barrier.

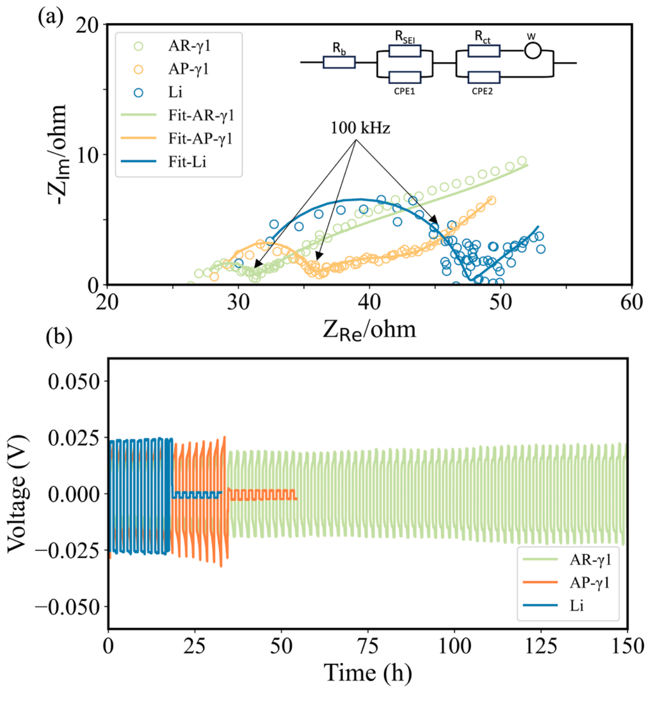

Fig. 4. (a) The Nyquist plots for AR-γ1, AP-γ1, and pure Li. (b) Voltage behavior of symmetric cells for AR-γ1, AP-γ1, and pure Li at the current density and areal capacity of 0.5 mA/cm^2 and 0.5 mAh/cm^2.

Table 1
Resistances obtained through equivalent circuit fitting of EIS data.

Phases	R_b (Ω)	R_{SEI} (Ω)	R_{ct} (Ω)
AR-γ1	27.27	3.69	14.53
AP-γ1	28.60	5.53	8.80
Li	30.68	16.72	0.09

Here, E_{vac} represents the total energy of the model containing a Li vacancy, and E_{bulk} corresponds to the total energy of the model without Li vacancy.

2.3. Surface energy computation

Surface energy (γ) measures the energy difference between a freshly generated surface and the corresponding bulk structure, [38,39] which offers critical insights into the surface's stability and reactivity. The formula for surface energy is:

$$\gamma = (E_{slab} - E_{bulk}) / 2A \tag{3}$$

Here, E_{slab} is the total energy of the slab structure and A denotes the surface area. To investigate the surface energy of the three phases, supercell models of 2 × 2 × 2 or 3 × 3 × 3 were utilized, accompanied by a 12 Å vacuum layer along the Z direction to prevent interactions between adjacent slabs. We have constructed symmetric surfaces, including (100), (110), and (111) planes with different terminations. For more detailed information regarding the surface models, please refer to Figure S2 and Table S1 in the Supporting Information.

2.4. Adsorption energy computation

A Li atom was initially positioned 3 Å away from the surface at three

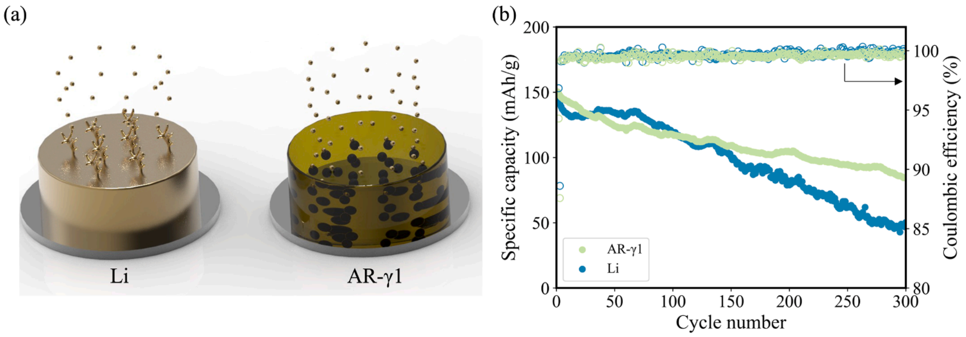

Fig. 5. (a) Charge-discharge behavior of AR-γ1 and Li. (b) The cycling performance of AR-γ1 and Li anode with LFP cathode at a current density of 0.4 mA/cm^2.

distinct adsorption sites (bridge, hollow, and top). The adsorption energy (E_{ads}) [40,41] of Li atom on the slab surface was determined using the following equation:

$$E_{ads} = E_{slab+Li} - E_{slab} - E_{Li} \tag{4}$$

Here, $E_{slab+Li}$ signifies the energy of the slab model with the Li atom adsorption, and E_{Li} stands for the energy per Li atom in the bulk material. Lower adsorption energy corresponds to stronger Li atom-surface binding, indicating a more stable adsorption configuration.

2.5. Li diffusion barrier

The diffusion barrier of Li is obtained by employing the nudged elastic band (NEB) [42,43] calculations. This method facilitates the identification of minimum-energy migration paths as well as the energy barrier associated with the diffusion process.

3. Experimental section

3.1. Synthesis of the Li-Ag alloy

The molten experiment was conducted in an argon-filled glovebox (Mikrouna), maintaining O_2 and H_2O levels below 0.01 ppm. In a standard procedure, fragments of Li metal foil were placed into a stainless steel crucible and heated on a hot plate to around 400 °C, generating molten Li. Subsequently, Ag power (Alfa Aesar, >99.99%) was introduced into the molten Li. To ensure thorough dispersion and uniform mixing, the mixture was manually stirred with a stainless steel stick for at least 30 minutes. Following this, the mixture was transferred onto a clean nickel plate for cooling and later sealed in plastic film. Two distinct atomic ratios of Li over Ag, specifically 11:1 (AR-γ1) and 20:1 (AP-γ1), were considered for the study. Finally, the AR-γ1 and AP-γ1 foils were fabricated through external rolling, outside the glovebox.

3.2. Synthesis of $LiFePO_4$ (LFP) cathode

For evaluating the electrochemical performance of the full cell, the LFP cathode was prepared using a conventional fabrication technique. This involved dispersing 0.8 g of LFP active powder (Macklin, battery-grade), along with 0.1 g Super P carbon black (Songjing Corp) and 0.1 g poly(vinylidene fluoride) (PVDF), in 4 mL of N-Methyl-2-pyrrolidone (NMP) solvent. The mixture was stirred on a magnetic stirrer for over 24 hours before being coated onto an aluminum foil using a scraper blade. Subsequently, the composite cathode was dried in a vacuum at 120 °C for more than 24 hours to eliminate any residual solvent.

3.3. Electrochemical characterization

Cell resistance was evaluated through electrochemical impedance spectroscopy (EIS) employing a Biologic VMP-3 system. The testing was conducted across a frequency range from 7 MHz to 100 mHz, utilizing a perturbation amplitude of 10 mV. The charge/discharge cycling was carried out by the LAND CT2001A battery tester at a current density of 0.4 mA cm^{-2} under a voltage range of 2.5–4.0 V. The CR2032-type coin cells were assembled in an argon-filled glovebox. LFP was employed as the cathode, polypropylene (5 μm-thick) as the separator, and either Li, AR-γ1, or AP-γ1 foil as the anode. To ensure uniform testing conditions, a standardized 60 μL of electrolyte was utilized in each coin cell. This electrolyte consisted of 1 M Li bis(trifluoromethane)sulfonamide (LiTFSI) dissolved in a mixture of 1,3-dioxolane (DOL) and 1,2-dimethoxyethane (DME) in a 1:1 v/v ratio.

4. Results and discussion

4.1. Phase diagram and crystal structure

As illustrated in Fig. 1a, the Li-Ag alloy phase diagram exhibits six distinct phases: α phase, β phase, γ3 phase, γ2 phase, γ1 phase, and δ phase. [30,44] Within the realm of Li-Ag alloys, the Li-rich composition holds considerable promise to yield a notably high energy density, garnering specific focus on the γ1 phase. Meanwhile, the γ1 and δ phase were reported in previous studies. [45–48] The structural configurations of AR-γ1, AP-γ1, and pure Li represent the Ag-rich and Ag-poor γ1 phase and δ phase, as depicted in Fig. 1b-d, respectively.

4.2. Thermodynamic stability

Assessing thermodynamic stability provides insights into material stability and reaction trends, playing a crucial role in material design and performance prediction. [51] We performed calculations to assess the thermodynamic stability of AR-γ1, AP-γ1, and Li based on formation energy, which are −0.028 eV/atom, −0.017 eV/atom, and 0 eV/atom, respectively, as shown in Fig. 2a. These findings suggest that the AR-γ1 possesses the highest thermodynamic stability. The heat map presented in Fig. 2b depicts the calculated reaction energy between AR-γ1, AP-γ1, Li, and six solid-state electrolytes, namely, $Li_{10}GeP_2S_{12}$, $Li_{1.3}Al_{0.3}Ti_{1.7}(PO_4)_3$, Li_6PS_5Cl, Li_3InCl_6, $Li_2La_2Ti_3O_{10}$, and $Li_7La_3Zr_2O_{12}$. Notably, all three phases display relatively low reaction energies (−15 to −14 meV/atom) when paired with $Li_7La_3Zr_2O_{12}$. Conversely, the reaction energies between these three anodes and $Li_{10}GeP_2S_{12}$, $Li_{1.3}Al_{0.3}Ti_{1.7}(PO_4)_3$, Li_6PS_5Cl, Li_3InCl_6, and $Li_2La_2Ti_3O_{10}$ range from −660 to −127 meV/atom, implying potential chemical reaction at the interface. Among the three phases, AR-γ1 exhibits the highest compatibility with solid-state electrolytes, making it a promising candidate for advanced battery applications. On the other hand, vacancies exert a significant influence on a material's physical, mechanical, and thermodynamic properties, including diffusion, specific heat, and Young's modulus. [52] Hence, employing DFT calculations, we assessed the vacancy formation energy for AR-γ1, AP-γ1, and pure Li using Eq. (2), as depicted in Figure S1. Remarkably, Li metal exhibits a higher Li vacancy formation energy than Li-Ag alloys, with AR-γ1 displaying a higher vacancy formation energy than AP-γ1. This distinction might play a role in the observed enhancement of the Li diffusion coefficient in Li-Ag alloys when compared to pure Li. [30,53]

4.3. Surface energy, adsorption energy, and diffusion barrier

Prior to investigating the influence of lithiophilic sites during Li plating on AR-γ1, AP-γ1, and pure Li surfaces, the surface energy is computed to identify the most stable surface facet. Fig. 3a highlights that the (100) facet is the most stable surface orientation for AR-γ1, AP-γ1, and pure Li, as denoted by the asterisk (*). The respective surface energy values are 0.423, 0.439, and 0.445 J/m^2. Details regarding other surface models and energies can be found in Table S1. Consequently, the (100) crystal facets are selected for Li adsorption calculations. In Fig. 3b, the hollow site emerges as the preferred adsorption location, while top and bridge sites are also possible. Detailed adsorption energy values are listed in Table S2. For AR-γ1, AP-γ1, and pure Li, the Li adsorption energies (E_{ads}) at hollow sites are −1.293, −0.987, and −0.702 eV, respectively. These results indicate that AR-γ1 and AP-γ1 exhibit lower adsorption energies than pure Li, with AR-γ1 showing the lowest E_{ads}. This observation suggests that Li-Ag alloys tend to have stronger Li adsorption onto the surface, and Li adsorbed on AR-γ1's surface is particularly stable. Due to Ag's affinity for Li, the Li diffusion barriers in Li-Ag alloys are theoretically lower than pure Li. As depicted in Fig. 3c, energy barriers for Li diffusion are 0.105, 0.139, and 0.295 eV for AR-γ1, AP-γ1, and Li, respectively. Thus, AR-γ1 and AP-γ1 facilitate a more efficient Li transport rate than pure Li. Due to the small diffusion energy barrier and excellent electronic conduction properties exhibited by the AR-γ1 alloy, herein, the AR-γ1 alloy demonstrates exceptional ionic and electronic transport channels.

4.4. Experiment performance

AR-γ1 and AP-γ1 have been characterized using XRD (Figure S2) and SEM (Figures S3 and S4). As depicted in Figure S2, the XRD peaks of AP-γ1 are consistent with those reported by Jin et al. [30] AR-γ1 is composed of mixed phases, including the γ1 phase and Li_9Ag_4 phase. The peak for Cu phase are from the Cu substrate. The SEM images in Figure S3a-b and Figure S4a-b reveal that the surfaces of AR-γ1 and AP-γ1 are smooth. Additionally, the corresponding surface and cross-section EDS maps (Figure S3c,f and Figure S4c,f) for AR-γ1 and AP-γ1, demonstrate the uniform distribution of Ag elements across the foil. Additionally, in Figure S3e and Figure S4e, the thickness of AR-γ1 and AP-γ1 falls within the range of 50–60 μm, showing promise for achieving high energy density.

Electrochemical Impedance Spectroscopy (EIS) [54–56] is an electrochemical characterization technique that involves measuring the impedance of a target system as a function of the frequency of a given sinusoidal waveform. EIS is utilized for the analysis and study of electrode kinetics and surface behaviors within the system. This non-invasive method is widely employed due to its capability to assess electrode dynamics without causing damage to the surface of the target system. Fig. 4a illustrates the typical EIS responses of AR-γ1, AP-γ1, and pure Li at 25°C. Table 1 provides the associated fitting parameters. Clearly, the values of R_{SEI} for AR-γ1 are considerably lower than those for AP-γ1 and pure Li, highlighting the favorable effect of minor Ag doping in enhancing interfacial kinetics and reducing the intrinsic impedance of pure Li. In addition, as depicted in Fig. 4b, The use of AR-γ1 in the symmetric cell results in the lowest polarization, providing significant stability over both AP-γ1 and pure Li. Additionally, AR-γ1 maintains stable voltage profiles for up to 150 hours, whereas the stability of AP-γ1 and pure Li is limited to approximately 35 and 20 hours, respectively. This indicates that AR-γ1 is less susceptible to dendrite growth compared to AP-γ1 and pure Li.

Based on the analysis above, it is evident that AR-γ1 possesses enhanced thermodynamic stability, improved adsorption energy, and superior Li diffusion properties. Additionally, it is noteworthy that AR-γ1 demonstrates lower impedance in comparison to AP-γ1 and pure Li, followed by AP-γ1. The charge-discharge behavior of AR-γ1 differs from that of pure Li. During lithiation, Li atoms are generated on the surface of the alloy and diffuse within the foil to form an alloy structure. Similarly, during delithiation, Li atoms produced through dealloying can be extracted from the foil similar to the discharge period. This behavior highlights efficient Li charge-discharge dynamics within the alloy. Due to the distinct charge-discharge behavior of AR-γ1 and pure Li, they exhibit different Li deposition morphologies. Fig. 5a illustrates the process of Li inward-growth plating into the AR-γ1 foil, effectively preventing surface deposition and the associated dendrite formation. In contrast, surface plating of Li on the Li metal anode leads to dendrite formation, posing potential safety concerns. Furthermore, to verify this analysis, long-term cycling tests were conducted. Cells employing AR-γ1 and pure Li as anodes, with LFP as the cathode, were examined at a current density of 0.4 mA/cm^2, as shown in Fig. 5b. After 300 cycles, the AR-γ1 cell exhibits significantly less capacity fading compared to pure Li. Specifically, the specific capacity of AR-γ1 fades from 150.3 to 84.7 mAh/g, whereas that of pure Li decreases from 147.5 to 50.2 mAh/g. The average Coulombic efficiency for both AR-γ1 and pure Li exceeds 99% over 300 cycles. The extended cycling of the cells further verify that AR-γ1 outperforms pure Li. Additionally, cells with AR-γ1 and AP-γ1 as anodes were also compared. The testing was performed by applying 0.1 mA/cm^2 for the first two cycles and 0.4 mA/cm^2 for the subsequent cycles, with the mass loading of cathode active material at 3.0 mg/cm^2. As shown in Figure S6. the average coulombic efficiencies for AR-γ1 and AP-γ1 are 99.92% and 99.01%, respectively. Additionally, the specific capacities of AR-γ1 and AP-γ1 are comparable, with AR-γ1 slightly exceeding AP-γ1.

5. Conclusions

In this study, we employed a combination of DFT calculations and experimental analysis to compare the performance of AR-γ1, AP-γ1, and pure Li anodes. Firstly, we identified that AR-γ1 exhibits superior thermodynamic stability compared to AP-γ1 and pure Li. Secondly, we investigated the Li adsorption energy and Li diffusion barriers for these phases, revealing that AR-γ1 outperforms AP-γ1 and pure Li. Finally, through EIS and symmetric cell tests, we unveiled the advantages of AR-γ1 as anode. Overall, our findings suggest that, within the γ1 phase, selecting the AR-γ1 is essential for balancing high energy density and electrochemical performance. This study provides valuable guidance for the selection and application of high-energy density phases in other alloy systems, offering innovative approaches to enhance the performance of Li-ion batteries.

Declaration of Competing Interest

The authors declare that they have no known competing financial interests or personal relationships that could have appeared to influence the work reported in this paper.

Acknowledgments

This work was supported by National Natural Science Foundation of China (52072240), and the Materials Genome Initiative Center at Shanghai Jiao Tong University. All simulations were carried out with computational resources from Shanghai Jiao Tong University High Performance Computing Center.

Appendix A. Supporting information

Supplementary data associated with this article can be found in the online version at doi:10.1016/j.nxmate.2024.100188.

References

[1] L. Fu, et al., A Li3P nanoparticle dispersion strengthened ultrathin Li metal electrode for high energy density rechargeable batteries, Nano Res (2024) 1–8.

[2] Y. Zhuang, et al., Understanding the Li diffusion mechanism and positive effect of current collector volume expansion in anode free batteries*, Chin. Phys. B 29 (2020) 068202.

[3] G.-X. Li, et al., A superior carbonate electrolyte for stable cycling Li metal batteries using high Ni cathode, ACS Energy Lett. 7 (2022) 2282–2288.

[4] Y. Chen, et al., Mechanistic exploration of dendrite growth and inhibition for lithium metal batteries, Energies 16 (2023) 3745.

[5] B. Liu, J.-G. Zhang, W. Xu, Advancing lithium metal batteries, Joule 2 (2018) 833–845.

[6] X. Zhang, A. Wang, X. Liu, J. Luo, Dendrites in lithium metal anodes: suppression, regulation, and elimination, Acc. Chem. Res. 52 (2019) 3223–3232.

[7] J. Xiao, How lithium dendrites form in liquid batteries, Science 366 (2019) 426–427.

[8] J. Wang, et al., Toward dendrite-free metallic lithium anodes: from structural design to optimal electrochemical diffusion kinetics, ACS Nano 16 (2022) 17729–17760.

[9] Y. Zhao, Y. Wu, H. Liu, S.-L. Chen, S.-H. Bo, Accelerated growth of electrically isolated lithium metal during battery cycling, ACS Appl. Mater. Interfaces 13 (2021) 35750–35758.

[10] Y. Li, et al., How can the electrode influence the formation of the solid electrolyte interface? ACS Energy Lett. 6 (2021) 3307–3320.

[11] B. Li, et al., A review of solid electrolyte interphase (SEI) and dendrite formation in lithium batteries, Electrochem. Energy Rev. 6 (2023) 7.

[12] K. Song, et al., Ultrathin CuF2-rich solid-electrolyte interphase induced by cation-tailored double electrical layer toward durable sodium storage, Angew. Chem. 135 (2023) e202216450.

[13] C. Wei, et al., Synergistic surface and bulk engineering with Li-rich dual-phase Li-Al alloy anode for rational regulation of lithium deposition, J. Alloy. Compd. 960 (2023) 170643.

[14] C. Yang, et al., An electron/ion dual-conductive alloy framework for high-rate and high-capacity solid-state lithium-metal batteries. Adv. Mater. 31 (2019) 1804815.

[15] X. Wang, et al., Li plating on alloy with superior electro-mechanical stability for high energy density anode-free batteries, Energy Storage Mater. 49 (2022) 135–143.

[16] Y. Zhang, et al., Polyacrylonitrile fibers network reinforced polymer electrolyte with Li-Sn alloy layer protected Li anode toward ultra-long cycle lifespan for room-temperature solid-state batteries, Chem. Eng. J. 461 (2023) 141993.

[17] Z. Guo, et al., Combining solid solution strengthening and second phase strengthening for thinning Li metal foils, ACS Nano 17 (2023) 14136–14143.

[18] B. Li, et al., Dual Protection of a Li–Ag Alloy Anode for All-Solid-State Lithium Metal Batteries with the Argyrodite Li6PS5Cl Solid Electrolyte, ACS Appl. Mater. Interfaces 14 (2022) 37738–37746.

[19] S. Jiang, et al., In-situ construction of a hybrid interfacial protective layer for highly stable Li metal anodes, Mater. Today Energy 38 (2023) 101444.

[20] X.-M. Zheng, et al., An electrodeposition strategy for the controllable and cost-effective fabrication of Sb-Fe-P anodes for Li ion batteries, Electrochim. Acta 309 (2019) 469–476.

[21] D. Aurbach, et al., Attempts to improve the behavior of Li electrodes in rechargeable lithium batteries, J. Electrochem. Soc. 149 (2002) A1267.

[22] G.X. Wang, et al., Nanocrystalline NiSi alloy as an anode material for lithium-ion batteries, J. Alloy. Compd. 306 (2000) 249–252.

[23] Y. Ye, et al., Solid-solution or intermetallic compounds: phase dependence of the Li-alloying reactions for Li-metal batteries, J. Am. Chem. Soc. 145 (2023) 24775–24784.

[24] H.J. Choi, et al., In situ formed Ag-Li intermetallic layer for stable cycling of all-solid-state lithium batteries, Adv. Sci. 9 (2022) 2103826.

[25] B. Pang, et al., Ag nanoparticles incorporated interlayer enables ultrahigh critical current density for Li6PS5Cl-based all-solid-state lithium batteries, J. Power Sources 563 (2023) 232836.

[26] Y. Zhao, et al., Bottom-up lithium growth guided by Ag concentration gradient in 3D PVDF framework towards stable lithium metal anode, J. Energy Chem. 65 (2022) 666–673.

[27] Z. Zuo, et al., Lithiophilic silver coating on lithium metal surface for inhibiting lithium dendrites, Front. Chem. 8 (2020).

[28] S. Iwamura, et al., Li-rich Li-Si alloy as a lithium-containing negative electrode material towards high energy lithium-ion batteries, Sci. Rep. 5 (2015) 8085.

[29] S.H. Choi, et al., Marginal magnesium doping for high-performance lithium metal batteries. Adv. Energy Mater. 9 (2019) 1902278.

[30] S. Jin, et al., Solid–solution-based metal alloy phase for highly reversible lithium metal anode. J. Am. Chem. Soc. 142 (2020) 8818–8826.

[31] D.S. Sholl, J.A. Steckel, Density Functional Theory: A Practical Introduction, John Wiley & Sons, 2022.

[32] G. Kresse, J. Hafner, Ab initio molecular dynamics for liquid metals, Phys. Rev. B 47 (1993) 558–561.

[33] G. Kresse, J. Furthmüller, Efficient iterative schemes for ab initio total-energy calculations using a plane-wave basis set, Phys. Rev. B 54 (1996) 11169–11186.

[34] G. Kresse, J. Furthmüller, Efficiency of ab-initio total energy calculations for metals and semiconductors using a plane-wave basis set, Comput. Mater. Sci. 6 (1996) 15–50.

[35] M. Mayo, A.J. Morris, Structure prediction of Li–Sn and Li–Sb intermetallics for lithium-ion batteries anodes. Chem. Mater. 29 (2017) 5787–5795.

[36] Y. Feng, et al., High-throughput modeling of atomic diffusion migration energy barrier of fcc metals, Prog. Nat. Sci.: Mater. Int. 29 (2019) 341–348.

[37] C.-T. Yang, Y. Qi, Maintaining a flat Li surface during the Li stripping process via interface design, Chem. Mater. 33 (2021) 2814–2823.

[38] V. Pande, V. Viswanathan, Computational screening of current collectors for enabling anode-free lithium metal batteries, ACS Energy Lett. 4 (2019) 2952–2959.

[39] Y. He, et al., Discovery of an unexpected metal dissolution of thin-coated cathode particles and its theoretical explanation, Adv. Theory Simul. 3 (2020) 2000002.

[40] Y. He, et al., Regulation of dendrite-free Li plating via lithiophilic sites on lithium-alloy surface, ACS Appl. Mater. Interfaces 14 (2022) 33952–33959.

[41] X. Gao, et al., Fast ion transport in Li-rich alloy anode for high-energy-density all solid-state lithium metal batteries, Adv. Funct. Mater. 33 (2023) 2209715.

[42] Z.-M. Xu, S.-H. Bo, H. Zhu, $LiCrS_2$ and $LiMnS_2$ cathodes with extraordinary mixed electron–ion conductivities and favorable interfacial compatibilities with sulfide electrolyte, ACS Appl. Mater. Interfaces 10 (2018) 36941–36953.

[43] G. Henkelman, B.P. Uberuaga, H. Jónsson, A climbing image nudged elastic band method for finding saddle points and minimum energy paths, J. Chem. Phys. 113 (2000) 9901–9904.

[44] C.-M. Park, H. Jung, H.-J. Sohn, Electrochemical behaviors and reaction mechanism of nanosilver with lithium, Electrochem. Solid-State Lett. 12 (2009) A171.

[45] X. Zhong, et al., Predicted stable structures of the Li–Ag system at high pressures, J. Phys. Chem. Lett. 12 (2021) 1671–1675.

[46] S. Li, et al., Unveiling the stress-buffering mechanism of deep lithiated ag nanowires: a polymer segmental motion strategy toward ultra-robust li metal anodes, Adv. Funct. Mater. 32 (2022) 2203010.

[47] A.D. Pelton, The Ag−K (Silver-Potassium) system, 223–223, Bull. Alloy Phase Diagr. 7 (1986), 223–223.

[48] C. Zhou, C. Guo, C. Li, Z. Du, Thermodynamic optimization of the Li–Pb system aided by first-principles calculations. J. Nucl. Mater. 477 (2016) 95–101.

[49] H. Okamoto, et al., Binary alloy phase diagrams, ASM International 12 (1990) 3528–3531.

[50] K. Momma, F. Izumi, VESTA 3 for three-dimensional visualization of crystal, volumetric and morphology data, J. Appl. Cryst. 44 (2011) 1272–1276.

[51] Y. Yang, et al., Activating the paddle-wheel effect towards lower temperature in a new sodium-ion solid electrolyte, $Na_{3.5}Si_{0.5}P_{0.5}Se_4$, J. Mater. Chem. A 11 (2023) 9555–9565.

[52] S.D. Miller, J.R. Kitchin, Relating the coverage dependence of oxygen adsorption on Au and Pt fcc(111) surfaces through adsorbate-induced surface electronic structure effects, Surf. Sci. 603 (2009) 794–801.

[53] J. Mao, et al., Graphene aerogels for efficient energy storage and conversion, Energy Environ. Sci. 11 (2018) 772–799.

[54] Y. Huang, et al., Surface coating with Li-Ti-O to improve the electrochemical performance of Ni-rich cathode material, Appl. Surf. Sci. 489 (2019) 913–921.

[55] Z. Wang, et al., Tailoring lithium concentration in alloy anodes for long cycling and high areal capacity in sulfide-based all solid-state batteries, eScience 3 (2023) 100087.

[56] W. Jing, et al., Li-Indium alloy anode for high-performance Li-metal batteries, J. Alloy. Compd. 924 (2022) 166517.